

pubs.acs.org/NanoLett Letter

# Enhancing Infrared Light-Matter Interaction for Deterministic and Tunable Nanomachining of Hexagonal Boron Nitride

Fernand E. Torres-Davila, Michael Molinari, Richard G. Blair, Nabil Rochdi, and Laurene Tetard\*



Cite This: Nano Lett. 2022, 22, 8196-8202



**Read Online** 

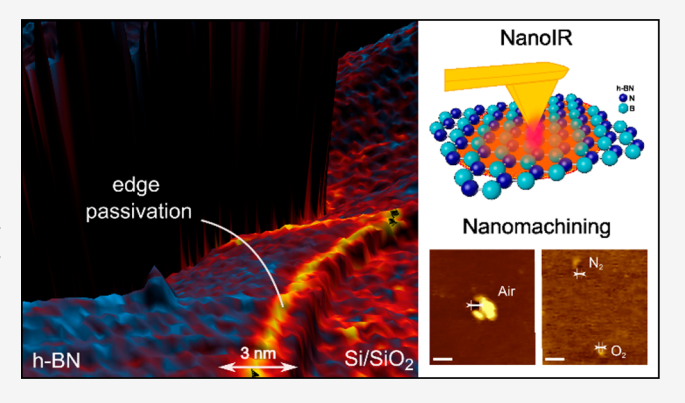
**ACCESS** 

III Metrics & More

Article Recommendations

Supporting Information

**ABSTRACT:** Tailoring two-dimensional (2D) materials functionalities is closely intertwined with defect engineering. Conventional methods do not offer the necessary control to locally introduce and study defects in 2D materials, especially in non-vacuum environments. Here, an infrared pulsed laser focused under the metallic tip of an atomic force microscope cantilever is used to create nanoscale defects in hexagonal boron nitride (*h*-BN) and to subsequently investigate the induced lattice distortions by means of nanoscale infrared (nano-IR) spectroscopy. The effects of incoming light power, exposure time, and environmental conditions on the defected regions are considered. Nano-IR spectra complement the morphology maps by revealing changes in lattice vibrations that distinguish the defects formed under various environments. This work introduces versatile experimental avenues



to trigger and probe local reactions that functionalize 2D materials through defect creation with a higher level of precision for applications in sensing, catalysis, optoelectronics, quantum computing, and beyond.

KEYWORDS: nanomachining, light-matter interaction, nano-infrared spectroscopy, 2D materials, defect engineering

redicted electronic properties of two-dimensional (2D) graphene,<sup>1,2</sup> transition metal dichalcogenides,<sup>3</sup> and hexagonal boron nitride (h-BN)4 have bolstered interest in 2D materials from fundamental and applied viewpoints. While their impact on the performance of energy devices has been widely demonstrated, 5-7 emerging functionalities have been conferred to 2D materials while maintaining their conformation merits, as in the case of defect-mediated growth of graphene hybrid structures,8 Moiré assemblies in stacked 2D layers,9 or engineered defects in h-BN.10 Introducing defects offers new routes to engineer 2D materials for optoelectronics, catalysis, and quantum information applications. For instance, defect-laden h-BN (dh-BN) exhibits catalytic activity enabling olefins hydrogenation 11 as well as CO2 capture and conversion. 12 Moreover, selected defects in h-BN display quantum properties at room temperature, 13 thus providing a new platform to elaborate 2D quantum devices. 14,15 More recently, theoretical models predicted that strongly correlated electronic regimes can be introduced in h-BN by undulations of the monolayers exhibiting nonzero Gaussian curvature. 16 Such experimental manipulations of 2D layers will require to pattern structural distortions that can be tuned at selected locations and to monitor chemical alterations of the material undergoing structural and chemical changes.<sup>17</sup>

Apart from those inherently induced by exfoliation, defects in h-BN are commonly created by ionic bombardment, <sup>18</sup> plasma etching, <sup>19</sup> electronic irradiation, thermal annealing, <sup>20</sup> or

mechanical processing. <sup>11</sup> These techniques are energyintensive and result in defects formation throughout the surface, hindering rigorous investigation of individual features. In addition, the reactivity of induced defects is generally assessed using standard analytical methods, such as optical spectroscopy, X-ray photoemission spectroscopy, or mass spectrometry. All these techniques provide averaged information about the probed volume (in the cubic micrometers range) that encompasses a large area of undisturbed material.

Means to isolate the signature of a local defect and its effect on the material local properties are currently lagging. While tools with nanoscale resolving power, such as transmission electron microscopy (TEM), can provide an ultrahighresolution view of materials lattice structure and changes, <sup>21–23</sup> their use for *in situ* chemical analysis of 2D systems has been challenging. <sup>24</sup> Furthermore, *in vacuo* spectroscopy performed in the TEM generally provides elemental analysis of materials, but not the chemical picture needed to understand local reactions taking place at defect sites. The nature of defects can

Received: July 19, 2022 Revised: September 14, 2022

Published: September 19, 2022





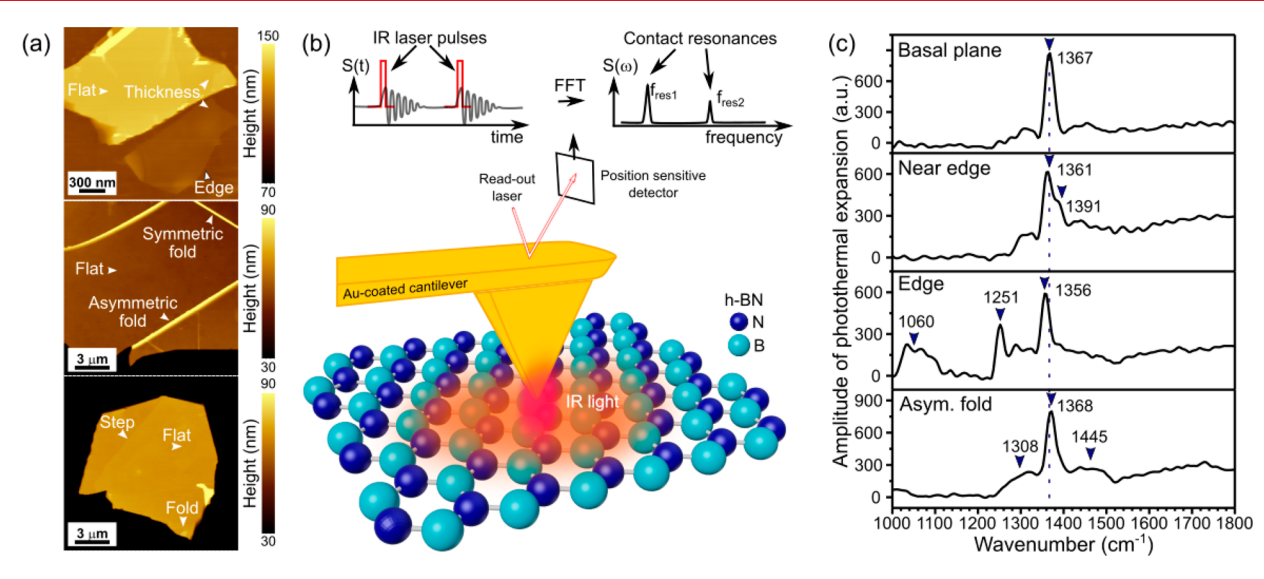


Figure 1. Nano-IR processing and characterization of localized defects in h-BN. (a) AFM topography images of exfoliated h-BN displaying the various regions and common large defects, various thicknesses, and unaffected flat regions. (b) Nano-IR scheme used for defect formation and analysis. The infrared pulsed laser is focused on the Au-coated AFM tip apex. (c) Nano-IR spectra collected at various deformations of the h-BN flakes showing the main vibrational mode  $\sim 1367$  cm<sup>-1</sup> in pristine h-BN and its shifts attributed to the different probed deformations.

be assessed by measuring their density of states (DOS) by scanning tunneling microscopy, <sup>25–27</sup> but vacuum constraints prevent most *in operando* analyses. In addition, metallic substrates should be used under wide-bandgap 2D monolayers, which can affect the material's reactivity. <sup>28</sup> On the other hand, other scanning probe microscopy (SPM) methods combine nanoscale resolution and high performance in non-vacuum environments, with the possibility to probe functional properties. <sup>29,30</sup> SPM has also been used for nanolithography using electrical, mechanical or thermal processes, but the changes in chemical bonds occurring during defect formation remain elusive. <sup>31–33</sup> Improving the understanding of defect formation mechanisms, the evolution of their spatial footprint, and the interplay of these local variations with surrounding molecules calls for tools allowing functional analyses with enhanced spatiotemporal resolution.

Advances in functional SPM, such as nanoscale infrared (nano-IR) spectroscopy, 34 can be implemented under controlled conditions, though only a few experimental studies have monitored local chemical changes occurring at an active site. 35,36 We report here the first-time utilization of atomic force microscopy (AFM) and nano-IR spectroscopy to create and study local nanoscale lattice distortions in 2D materials. The phenomenon of light-assisted nanoscale defect creation in h-BN occurring at the vicinity of the AFM tip is introduced and investigated, including the effect of incoming light power, exposure time, and environmental conditions. Nano-IR spectroscopy is invoked to describe changes in chemical fingerprint associated with the defect creation. The local spectra reveal the formation of new bonds at defect sites, which are shown to depend on the local environment of the AFM tip. The measurements highlight the role oxygen and water molecules play in modifying the local properties of defectladen 2D materials. On the basis of these findings, we formulate requirements to consider for substrates selection and environmental conditions in view of conquering materialdesign rules for defect-mediated applications of 2D materials.

The topography of *h*-BN flakes (Figure 1a) represents common defects observed in exfoliated pristine 2D layers,

including edges, folds, and steps. Exfoliated flakes are laterally too small for individual analysis by conventional mid-IR spectroscopy; so are steps, folds, or wrinkles within them. Overall, the optically diffraction-limited spatial resolution of mid-IR light (several micrometers) prevents measuring the effect of localized defects on lattice vibrations. Similarly, when points of isolated lattice distortions affect the DOS close to the Fermi level to promote reactivity, 12 the related sorptions or chemical reactions cannot readily be monitored, given the limited number of molecules to probe. Nano-IR overcomes this limitation by analyzing the variations in h-BN IR fingerprints in the presence of lattice distortions using the AFM tip (Figure 1b). The material is excited with a pulsed IR laser focused on the tip engaged in contact mode with constant force feedback. The laser pulse frequency (1 kHz) is well below the cantilever free air and contact resonances (>10 kHz). The cantilever ringing vibrations resulting from each light pulse are recorded. The cantilever contact resonances are identified from fast Fourier transform of the cantilever signal S(t) (Figure 1b),<sup>37</sup> and their amplitudes are used to monitor the photothermal expansion of the excited volume underneath the tip.<sup>38</sup> Hereafter, nano-IR spectra (Figure 1c) are derived from the first contact resonance amplitude and correspond to the chemical composition of the probed volume (see Methods in the Supporting Information). We note that this approach is different from that used to perform nanoscale Fourier transform infrared (FTIR) measurements via a near-field scanning optical microscopy scheme, using the tip as a nanoantenna and deriving the results from theoretical treatments of optical signals. 39-41

The IR spectrum of the pristine *h*-BN basal plane (Figure 1c) consists of a single band at 1367 cm<sup>-1</sup> corresponding to the transverse optical (TO) phonon mode, which gradually red-shifts when approaching an edge (~1356 cm<sup>-1</sup> at the edge). Theoretical calculations have attributed a band bending region of ~2 nm from the edge with altered interatomic distance to this effect due to lower electron density near the basal plane edge. On folds, the TO band exhibits no substantial shift but an asymmetry due to features

at 1356 and 1379  $\rm cm^{-1}$  (Figure S2). Moreover, two smaller and broader bands detected on folds (1308 and 1445  $\rm cm^{-1}$ ) are attributed to regions of compressive and tensile strain in the fold.<sup>45</sup>

The nano-IR spectrum collected for a 3 nm thick flake (Figure 2a) on pristine regions (point 1 in Figure 2b) also

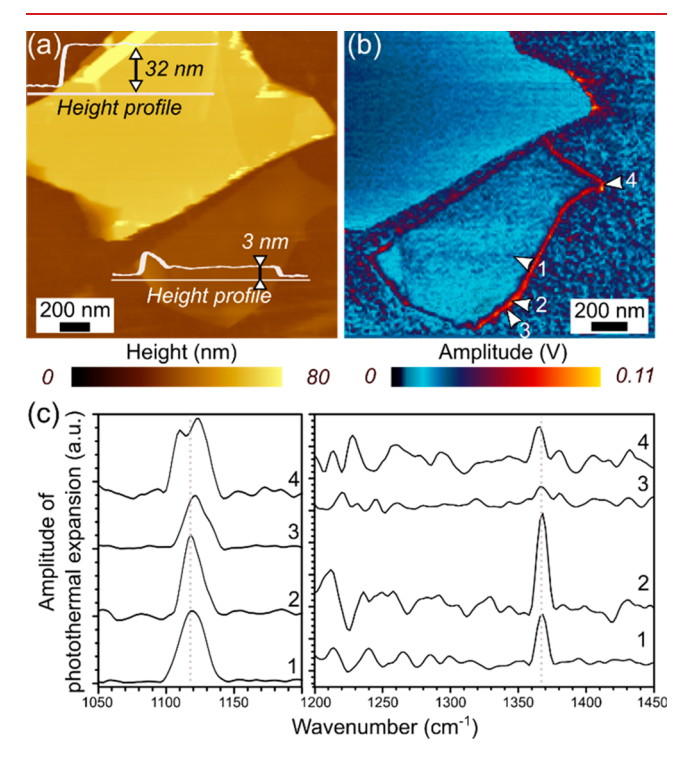


**Figure 2.** Nano-IR features of identified defects in exfoliated h-BN flakes. (a) AFM height image of two exfoliated h-BN flakes of thickness 32 and 3 nm, respectively. (b) Nano-IR image acquired at 1120 cm<sup>-1</sup> across the thick and thin flakes exfoliated on a Si substrate with a native SiO<sub>2</sub> layer. (c) Nano-IR spectra acquired at points 1, 2, 3, and 4 of the 3 nm thick flake, as marked in (b).

displays a band at 1367 cm<sup>-1</sup> (Figure 2c). The band position remains unchanged at different positions in the flake center, while its full width at half-maximum (FWHM) significantly decreases for thinner flakes (Figure S3). Another notable difference between thick (above 30 nm) and thin flakes (below 5 nm) is the band observed around 1120 cm<sup>-1</sup> (Figures 2c and S4). This band presents a greater intensity than the TO mode for the thinnest layer, and it is not observed for 50 nm thick flakes (Figure S4). Nano-IR spectra of the bare SiO<sub>2</sub>/Si substrate reveal prominent bands of in-phase asymmetric stretching of adjacent oxygen atoms and Si-OH deformation (1009 cm<sup>-1</sup>), 46,47 bulk out-of-plane asymmetric stretching of Si-O-Si (1107 cm<sup>-1</sup>), and Si-O bonds (1266 cm<sup>-1</sup>)<sup>48</sup> (Figure S5b). The band at ~1107 cm<sup>-1</sup> is not observed in conventional FTIR spectra. Nano-IR probes the sample surface with a penetration depth that depends on the material thermal properties but typically exceeds 50 nm. Thus, the volume probed by nano-IR is mainly composed of SiO<sub>2</sub>, while FTIR spectroscopy predominantly renders the Si bulk signal. The asymmetry of the peak at 1107 cm<sup>-1</sup> results from overlapping with the band at 1073 cm<sup>-1</sup> relative to in-phase Si-O stretching. 48,51 Other reported bands relative to Si-O-Si asymmetric stretching, due to Coulomb interaction-induced LO-TO splitting (1125 cm<sup>-1</sup>)<sup>52</sup> or oxidation of porous silicon

(1176 cm<sup>-1</sup>),<sup>49</sup> could be responsible for the smaller features (Figure S5b-ii). We infer that the band at 1120 cm<sup>-1</sup> originates from B–OH bonds formed as a result of the passivation of intrinsic defects during mechanical exfoliation and subsequent exposure to air.<sup>53</sup> Previous studies estimated densities of boron and nitrogen vacancies after mechanical exfoliation to about  $10^5$  and  $5 \times 10^3~\mu\text{m}^{-2}$ , respectively.<sup>10</sup> The signal difference between the 50 nm thick and the 3 nm thick flakes can then be interpreted by the increased ratio of surface defects over intact B–N bonds. Because only the surface layers are expected to experience defect creation during exfoliation, the proportion of defects in the 3 nm thick flake is larger than in the thicker flakes for which most of the core layers are expected to remain intact.

When recording the nano-IR map of a region encompassing both thick (32 nm) and thin (3 nm) layers with illumination at 1120 cm<sup>-1</sup> (Figure 2b), a strong signal is revealed at flakes edges and corners, which is predominant around the thinner flake. Nano-IR measurements at different points along edges underline enhanced photothermal expansion as compared to the basal plane and the SiO<sub>2</sub>/Si substrate (red to yellow regions of width <10 nm around the flakes in Figure 2b). Three-dimensional representation of the overlay of AFM topography and the nano-IR signal collected under the 1120 cm<sup>-1</sup> illumination (Figure S6) confirms that the strong nano-IR amplitude is located within the flake. In contrast with the pristine basal plane, nano-IR spectra collected at different points along the edge (marked 2, 3, and 4 in Figure 2c) reveal two distinct vibrational modes between 1100 and 1150 cm<sup>-1</sup> (Figure S7) that deviate from the previously identified SiO<sub>2</sub>/Si vibrations in the basal plane and edges signals (points 1, 2, and 3). At the corner (point 4), a prominent feature at 1108 cm<sup>-1</sup>, along with a weaker band at 1123 cm<sup>-1</sup>, could stem from the aforementioned bulk Si-O-Si asymmetric stretching. We attribute this change to the greater portion of the tip-sample contact being exposed to the SiO<sub>2</sub> substrate at corners. While the current spatial resolution of nano-IR spectroscopy cannot resolve atomic arrangements, the results suggest that flakes edges are passivated with B-OH bonds, though with varying local environments, especially at nonlinear cleavage regions (point 3) and corners (point 4). Theoretical models have considered numerous potential edge conformations in h-BN, in agreement with our experimental results. 54-56

These results constitute the first report of nanoscale chemical analysis of local defects and passivation along h-BN edges using nano-IR spectroscopy, which paves the way to exciting discussions about theoretical models. The findings also raise awareness on potential impacts of sample preparation and substrate selection on the nanoscale chemical fingerprint obtained by nano-IR spectroscopy. As such, nano-IR spectra of pristine h-BN on  $\text{SiO}_2/\text{Si}$  and on IR transparent substrates (Figure S8) are compared. IR transparent substrates, especially ZnS, offer a cleaner background in the  $1200-1600~\text{cm}^{-1}$  range (Figure S9). Therefore, all measurements presented hereafter were performed on h-BN flakes deposited on ZnS substrates.

Next, we demonstrate that selected illumination conditions of the nano-IR tip interacting with h-BN basal plane enables the controlled formation of local defects. For a 6 nm thick flake, nano-IR spectra performed in air at laser power of 0.1 mW exhibit the single TO mode of pristine h-BN (1367 cm $^{-1}$ ), indicating that the illumination conditions are below the threshold of defect formation. Immediately after a short exposure (few seconds) of the same point to pulses

corresponding to an output laser power of 0.8 mW, the nano-IR spectrum exhibits a shift of the prominent peak to 1360 cm<sup>-1</sup> and a secondary peak at 1386 cm<sup>-1</sup> (Figure 3d),

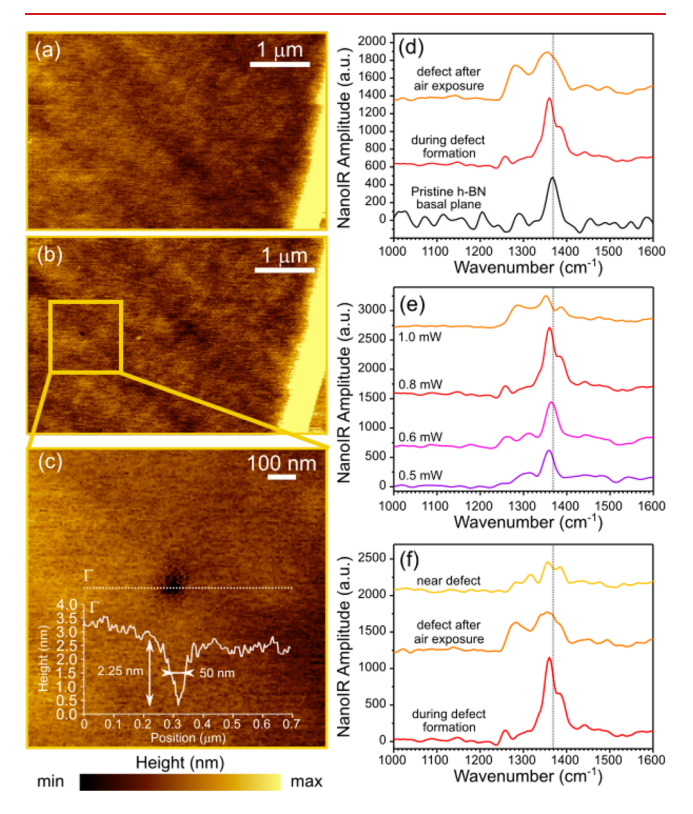


**Figure 3.** Nano-IR—AFM patterning of nanoholes in *h*-BN. (a, b) AFM topography of *h*-BN basal plane before (a) and after (b) laser-induced defect formation at 0.8 mW in air. (c) High-resolution AFM topography of the defect. The height profile of the laser-induced nanohole formed along Γ is presented as an inset, showing a full width at half-minimum of 50 nm and a depth of 2.25 nm. (d) Nano-IR spectra of the pristine basal plane before (black line), during (red line) and after (orange line) defect formation at the position corresponding to the center of the nanohole in (c). (e) Nano-IR spectra corresponding to defect formation obtained at laser power of 0.5 mW (purple line), 0.6 mW (pink line), 0.8 mW (red line), and 1.0 mW (orange line). (f) Nano-IR spectra collected at 0.8 mW at the center of the defect during formation (red line), after defect was exposed to air (orange line), and near the center of the defect after exposure to air (yellow line).

suggesting some strain in the lattice induced by illumination.<sup>45</sup> AFM topography images collected after the laser treatment reveal the formation of a nanohole about 2.25 nm deep and 50 nm in width (Figure 3b,c).

The defect spectral signature after exposure to air (several minutes), recorded with low laser power, contains significantly different features with two prevalent broad bands at 1280 and 1355 cm<sup>-1</sup> and a secondary shoulder at 1386 cm<sup>-1</sup> (Figure 3d). The band at 1280 cm<sup>-1</sup> is assigned to the TO mode in vitreous boron trioxide (ν-B<sub>2</sub>O<sub>3</sub>)<sup>57</sup> while vibrations at 1355 cm<sup>-1</sup> are ascribed to the asymmetric B–O stretch.<sup>58</sup> These suggest different environments are present at edges (B–OH) and in the vicinity (B–O) of the nanohole. The nano-IR spectrum collected away (several nanometers) from the nanohole edge (Figure 3f) shows that the lattice disruption extends to a region that depends on the illumination power

and remains, nonetheless, below  $\sim \! 100$  nm for laser power below 1.0 mW.

Increasing the laser power from 0.5 to 1.0 mW (Figure 3e) accelerates reactions with molecules from the water meniscus present at the tip–sample interaction region in ambient conditions. At 1.0 mW, bands from  $\nu$ -B<sub>2</sub>O<sub>3</sub> can already be resolved during the defect formation, suggesting that the reaction between deforming B–N bonds and reactive species (O<sub>2</sub> or H<sub>2</sub>O in air) could take place before or during the short illumination duration. Treatments performed at 1.0 and 1.3 mW not only formed B–O faster but also resulted in larger defects (Figure S10).

The significant size difference between the nanohole and the excited region ( $\sim$ 50–100  $\mu$ m, Figure S1) indicates that the defect formation in the h-BN basal plane originates from the interplay of light, interacting with the Au-coated tip, and its local environment. Indeed, the tip metallic coating is required since no defect or disruption of h-BN could be observed with conventional silicon nitride cantilevers of similar stiffness. Moreover, only illumination with wavenumbers close to 1367 cm<sup>-1</sup> leads to the formation of nanoholes that could be resolved by AFM (Figure S11). Overall, these observations suggest that the discovered light-induced nanoscale defect creation method in h-BN is promoted by charges polarization at the Au-coated cantilever tip, or hot electrons due to the lighting-rod effect,<sup>59</sup> together with vibrations from the TO phonon mode of the h-BN lattice, and the evolution of the reaction is influenced by the local environments.

At identical laser power, the nanoholes created under  $N_2$  are much smaller than those obtained in air (Figure 4). Tapping mode imaging of freshly formed defects maintained under N2 indicates the presence of two nanoholes similar to a doublewell around the tip position, which remained stable if not exposed to air. When reducing the exposure time, the doublewell formation was retained as well as the spacing between wells centers ( $\sim$ 43 nm), which corresponds to the diameter of the AFM tip. The smallest detected twin-defects were around 20 nm in diameter, separated by about 43 nm. However, imaging the same defect in contact mode renders the topography of a single nanobump (Figure S12). We infer that this atypical behavior may result from residual charges in the formed defect, strengthening the attractive van der Waals interaction in the tapping mode, while evacuated through the AFM tip in the contact mode.

We investigated changes in the chemical signature of the same defect site during and immediately after formation under N<sub>2</sub> at 1.0 mW, followed by exposure to air (Figure 5). The nano-IR spectrum presents a symmetric peak at 1351 cm<sup>-1</sup>, i.e., with a red shift similar to that of exfoliated flakes edges (Figure 1c). We found this shift to be a reliable indication of defects formation in the basal plane under the considered conditions. After defect formation, the nano-IR spectrum recorded in N<sub>2</sub> at low power shows that the band vanishes, highlighting the significant damage (i.e., deformation followed by nanohole formation) produced by the laser irradiation. After 10 min of exposure to air, two major bands located at 1366 and 1282 cm<sup>-1</sup> are observed. While the first band corresponds to *h*-BN, the band at 1282 cm<sup>-1</sup> is assigned to the TO mode of v-B<sub>2</sub>O<sub>3</sub>. <sup>57</sup> Hence, exposure to air brings about the local oxidation of h-BN and the lattice reconstructs in the form of a nanobump evolving over time. The absence of the band at 1120 cm<sup>-1</sup> indicative of B-OH in the previous measurements confirms the different nature of the B-O bond on the defect.

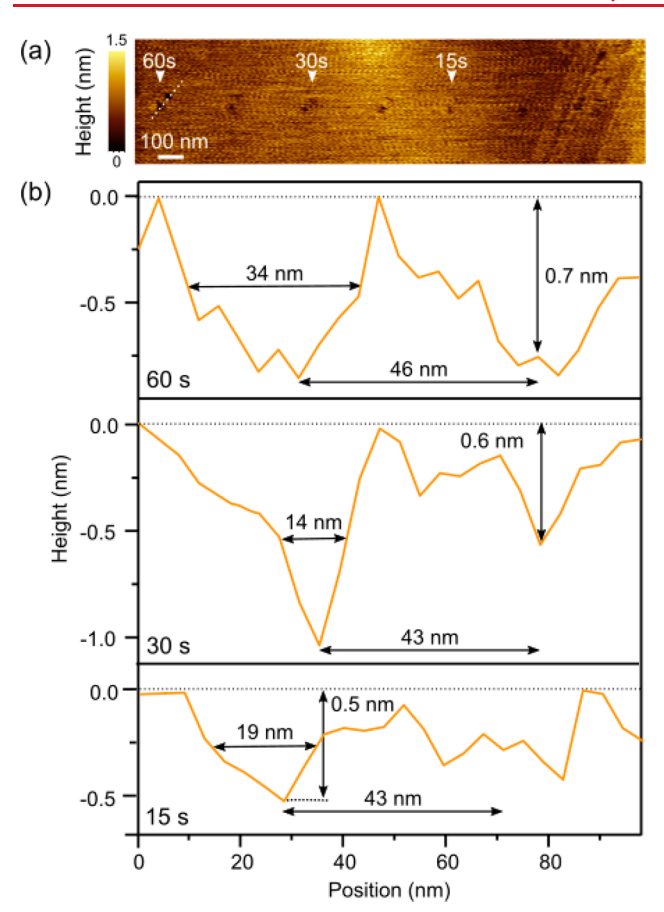


**Figure 4.** Nanomachining of local defects in h-BN under nitrogen. (a) Tapping mode topography image of defects created in h-BN under  $N_2$  using laser wavelength of 1368 cm $^{-1}$  at 0.24 mW. The exposure duration was varied from 60 to 15 s as indicated on the image. (b) Height profiles extracted from each defect.

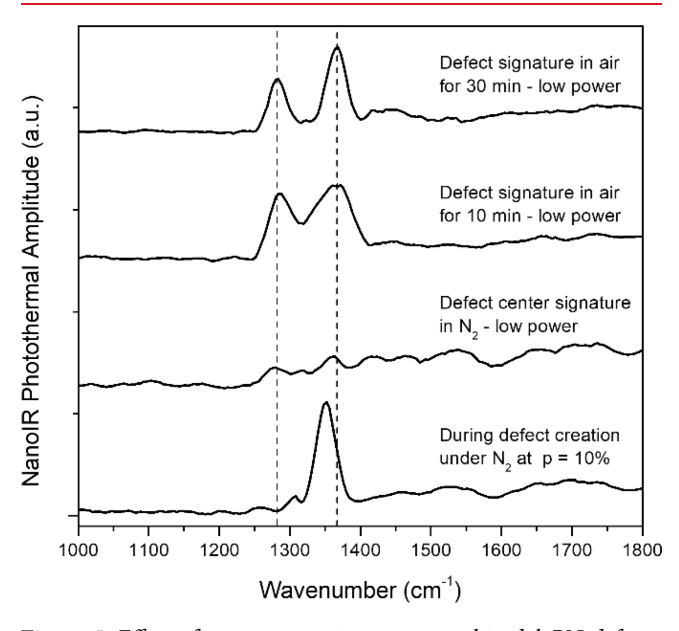


**Figure 5.** Effect of exposure to air on nanomachined *h*-BN defects. Nano-IR spectra acquired at the defect center: at 1.0 mW (p=10%) during defect creation under  $N_2$  atmosphere and at 0.1 mW after defect creation in  $N_2$  then after exposure to air for 10 and 30 min. The dashed lines indicate the positions of the bands centered at 1282 and 1366 cm<sup>-1</sup> after 30 min of exposure to air.

Lastly, nanoscale defects (FWHM  $\sim 22$  nm) are formed using the same parameters under  $O_2$ , though with a capped profile different from double-well structures obtained under  $N_2$  (Figure S13). The presence of oxygen leads to an immediate reaction with the BN lattice and features that are distinct from those created under oxygen-free environment and then exposed to air. The reaction of local defects with oxygen species is in agreement with reports about passivation of defect-laden h-BN along with evolving fluorescence upon exposure to air.

We have shown, for the first time, that nano-IR spectroscopy can be used to assign fingerprints to defects encountered in 2D h-BN flakes, including folds, edges, and sub-50 nm nanoholes. The infrared signatures collected provide rich information about the strain level in the lattice and deformation due to the disruption of the honeycomb lattice and/or the passivation by hydroxyl bonds. Furthermore, the ability of manipulating light-matter interaction at an AFM tip is revealed. Overall, the light-assisted method enables the introduction of defects into the h-BN basal plane and provides a powerful approach for defect engineering in other 2D materials, with a level of spatial, morphological, and chemical control that cannot be attained with conventional defect engineering methods. Morphology and chemical makeup of engineered defects can be tuned by laser power, wavelength, exposure duration, and local environment. Furthermore, the findings unveil the important role of the water meniscus present under the AFM tip in ambient conditions. Beyond defect oxidation, it is expected that targeted hydroxylating and further defect functionalization will be possible by modifying the local environment composition. Lastly, we could monitor the evolution of the initial lattice deformation as it is exposed to different environments, which will provide an important feedback to improve ab initio theoretical models. On the basis of our observations, we infer that the herein unveiled nanomachining approach would enable a more deterministic control of dimensions and chemical properties of defects in 2D materials for targeted applications such as nanoelectronics, quantum sensing, and beyond.

# ASSOCIATED CONTENT

# Supporting Information

The Supporting Information is available free of charge at https://pubs.acs.org/doi/10.1021/acs.nanolett.2c02841.

Additional experimental details, materials, and methods, including Figures S1-S13 (PDF)

# AUTHOR INFORMATION

## **Corresponding Author**

Laurene Tetard — NanoScience Technology Center, University of Central Florida, Orlando, Florida 32826, United States; Physics Department, University of Central Florida, Orlando, Florida 32816, United States; Occid.org/0000-0003-1771-466X; Email: laurene.tetard@ucf.edu

#### Authors

Fernand E. Torres-Davila — NanoScience Technology Center, University of Central Florida, Orlando, Florida 32826, United States; Physics Department, University of Central Florida, Orlando, Florida 32816, United States Michael Molinari — Institute of Chemistry and Biology of

Aichael Molinari – Institute of Chemistry and Biology of Membranes and Nano-objects (CBMN), CNRS UMR 5248,

- IPB, Université de Bordeaux, 33607 Pessac, France; o orcid.org/0000-0001-9906-655X
- Richard G. Blair Florida Space Institute, University of Central Florida, Orlando, Florida 32826, United States; Renewable Energy and Chemical Transformations Cluster (REACT), University of Central Florida, Orlando, Florida 32816, United States
- Nabil Rochdi Laboratory of Innovative Materials, Energy and Sustainable Development (IMED-Lab) and Department of Physics, Faculty of Sciences Semlalia, Cadi Ayyad University, Marrakesh 40000, Morocco; orcid.org/0000-0002-7303-1065

Complete contact information is available at: https://pubs.acs.org/10.1021/acs.nanolett.2c02841

#### Funding

F.E.T.D., R.B., and L.T. acknowledge support from NSF CHE-1465105. F.E.T.D. and L.T. also acknowledge support from NSF CHE-1847830.

#### Notes

The authors declare no competing financial interest.

## REFERENCES

- (1) Novoselov, K. S.; Geim, A. K.; Morozov, S. V.; Jiang, D.; Katsnelson, M. I.; Grigorieva, I. V.; Dubonos, S. V.; Firsov, A. A. Two-dimensional gas of massless Dirac fermions in graphene. *Nature* **2005**, 438, 197.
- (2) Castro Neto, A. H.; Guinea, F.; Peres, N. M. R.; Novoselov, K. S.; Geim, A. K. The electronic properties of graphene. *Rev. Mod. Phys.* **2009**, *81* (1), 109–162.
- (3) Wang, Q. H.; Kalantar-Zadeh, K.; Kis, A.; Coleman, J. N.; Strano, M. S. Electronics and optoelectronics of two-dimensional transition metal dichalcogenides. *Nat. Nanotechnol.* **2012**, *7*, 699.
- (4) Liu, L.; Feng, Y. P.; Shen, Z. X. Structural and electronic properties of h-BN. *Phys. Rev. B* **2003**, *68* (10), 104102.
- (5) Huang, Y.-J.; Chen, H.-C.; Lin, H.-K.; Wei, K.-H. Doping ZnO Electron Transport Layers with MoS<sub>2</sub> Nanosheets Enhances the Efficiency of Polymer Solar Cells. ACS Appl. Mater. Interfaces 2018, 10 (23), 20196–20204.
- (6) Yu, Z.; Tetard, L.; Zhai, L.; Thomas, J. Supercapacitor electrode materials: nanostructures from 0 to 3 dimensions. *Energy Environ. Sci.* **2015**, 8 (3), 702–730.
- (7) Yi, F.; Ren, H.; Shan, J.; Sun, X.; Wei, D.; Liu, Z. Wearable energy sources based on 2D materials. *Chem. Soc. Rev.* **2018**, 47 (9), 3152–3188.
- (8) Pradhan, B.; Das, S.; Li, J.; Chowdhury, F.; Cherusseri, J.; Pandey, D.; Dev, D.; Krishnaprasad, A.; Barrios, E.; Towers, A.; Gesquiere, A.; Tetard, L.; Roy, T.; Thomas, J. Ultrasensitive and ultrathin phototransistors and photonic synapses using perovskite quantum dots grown from graphene lattice. *Sci. Adv.* **2020**, *6* (7), eaay5225.
- (9) He, F.; Zhou, Y.; Ye, Z.; Cho, S.-H.; Jeong, J.; Meng, X.; Wang, Y. Moiré Patterns in 2D Materials: A Review. ACS Nano 2021, 15 (4), 5944–5958.
- (10) Zhang, J.; Sun, R.; Ruan, D.; Zhang, M.; Li, Y.; Zhang, K.; Cheng, F.; Wang, Z.; Wang, Z.-M. Point defects in two-dimensional hexagonal boron nitride: A perspective. *J. Appl. Phys.* **2020**, *128* (10), 100902.
- (11) Nash, D. J.; Restrepo, D. T.; Parra, N. S.; Giesler, K. E.; Penabade, R. A.; Aminpour, M.; Le, D.; Li, Z.; Farha, O. K.; Harper, J. K.; Rahman, T. S.; Blair, R. G. Heterogeneous Metal-Free Hydrogenation over Defect-Laden Hexagonal Boron Nitride. *ACS Omega* **2016**, *1* (6), 1343–1354.
- (12) Chagoya, K. L.; Nash, D. J.; Jiang, T.; Le, D.; Alayoglu, S.; Idrees, K. B.; Zhang, X.; Farha, O. K.; Harper, J. K.; Rahman, T. S.; Blair, R. G. Mechanically Enhanced Catalytic Reduction of Carbon

- Dioxide over Defect Hexagonal Boron Nitride. ACS Sustainable Chem. Eng. 2021, 9 (6), 2447–2455.
- (13) Tran, T. T.; Bray, K.; Ford, M. J.; Toth, M.; Aharonovich, I. Quantum emission from hexagonal boron nitride monolayers. *Nat. Nanotechnol.* **2016**, *11* (1), 37–41.
- (14) Vogl, T.; Lecamwasam, R.; Buchler, B. C.; Lu, Y.; Lam, P. K. Compact Cavity-Enhanced Single-Photon Generation with Hexagonal Boron Nitride. *ACS Photonics* **2019**, *6* (8), 1955–1962.
- (15) Tran, T. T.; Wang, D.; Xu, Z.-Q.; Yang, A.; Toth, M.; Odom, T. W.; Aharonovich, I. Deterministic Coupling of Quantum Emitters in 2D Materials to Plasmonic Nanocavity Arrays. *Nano Lett.* **2017**, *17* (4), 2634–2639.
- (16) Gupta, S.; Yu, H.; Yakobson, B. I. Designing 1D correlated-electron states by non-Euclidean topography of 2D monolayers. *Nat. Commun.* **2022**, *13* (1), 3103.
- (17) Bell, A. T. The Impact of Nanoscience on Heterogeneous Catalysis. *Science* **2003**, 299 (5613), 1688.
- (18) Peter, R.; Bozanic, A.; Petravic, M.; Chen, Y.; Fan, L.-J.; Yang, Y.-W. Formation of defects in boron nitride by low energy ion bombardment. *J. Appl. Phys.* **2009**, *106*, No. 083523.
- (19) Xu, Z. Q.; Elbadawi, C.; Tran, T. T.; Kianinia, M.; Li, X.; Liu, D.; Hoffman, T. B.; Nguyen, M.; Kim, S.; Edgar, J. H.; Wu, X.; Song, L.; Ali, S.; Ford, M.; Toth, M.; Aharonovich, I. Single photon emission from plasma treated 2D hexagonal boron nitride. *Nanoscale* **2018**, *10* (17), 7957–7965.
- (20) Choi, S.; Tran, T. T.; Elbadawi, C.; Lobo, C.; Wang, X.; Juodkazis, S.; Seniutinas, G.; Toth, M.; Aharonovich, I. Engineering and Localization of Quantum Emitters in Large Hexagonal Boron Nitride Layers. ACS Appl. Mater. Interfaces 2016, 8 (43), 29642–29648
- (21) van der Wal, L. I.; Turner, S. J.; Zečević, J. Developments and advances in in situ transmission electron microscopy for catalysis research. *Catalysis Science & Technology* **2021**, *11* (11), 3634–3658.
- (22) Hwang, S.; Chen, X.; Zhou, G.; Su, D. In Situ Transmission Electron Microscopy on Energy-Related Catalysis. *Adv. Energy Mater.* **2020**, *10* (11), 1902105.
- (23) He, B.; Zhang, Y.; Liu, X.; Chen, L. In-situ Transmission Electron Microscope Techniques for Heterogeneous Catalysis. *ChemCatChem* **2020**, *12* (7), 1853–1872.
- (24) Kamatani, K.; Higuchi, K.; Yamamoto, Y.; Arai, S.; Tanaka, N.; Ogura, M. Direct observation of catalytic oxidation of particulate matter using in situ TEM. *Sci. Rep.* **2015**, *5*, 10161.
- (25) Amara, H.; Latil, S.; Meunier, V.; Lambin, P.; Charlier, J. C. Scanning tunneling microscopy fingerprints of point defects in graphene: A theoretical prediction. *Phys. Rev. B* **2007**, *76* (11), 115423.
- (26) Wong, D.; Velasco, J.; Ju, L.; Lee, J.; Kahn, S.; Tsai, H.-Z.; Germany, C.; Taniguchi, T.; Watanabe, K.; Zettl, A.; Wang, F.; Crommie, M. F. Characterization and manipulation of individual defects in insulating hexagonal boron nitride using scanning tunnelling microscopy. *Nat. Nanotechnol.* **2015**, *10* (11), 949–953.
- (27) Ziatdinov, M.; Dyck, O.; Li, X.; Sumpter, B. G.; Jesse, S.; Vasudevan, R. K.; Kalinin, S. V. Building and exploring libraries of atomic defects in graphene: Scanning transmission electron and scanning tunneling microscopy study. *Science advances* **2019**, *5* (9), eaaw8989—eaaw8989.
- (28) Lyalin, A.; Nakayama, A.; Uosaki, K.; Taketsugu, T. Functionalization of Monolayer h-BN by a Metal Support for the Oxygen Reduction Reaction. *J. Phys. Chem. C* **2013**, *117* (41), 21359–21370.
- (29) Bang, J. J.; Russell, S. R.; Rupp, K. K.; Claridge, S. A. Multimodal scanning probe imaging: nanoscale chemical analysis from biology to renewable energy. *Analytical Methods* **2015**, *7* (17), 7106–7127.
- (30) Bian, K.; Gerber, C.; Heinrich, A. J.; Müller, D. J.; Scheuring, S.; Jiang, Y. Scanning probe microscopy. *Nature Reviews Methods Primers* **2021**, *1* (1), 36.
- (31) Garcia, R.; Knoll, A. W.; Riedo, E. Advanced scanning probe lithography. *Nat. Nanotechnol.* **2014**, *9* (8), 577–587.

- (32) Rochdi, N.; Tonneau, D.; Jandard, F.; Dallaporta, H.; Safarov, V. Fabrication and electrical properties of ultra-thin silicon nanowires. *physica status solidi (a)* **2008**, *205* (5), 1157–1161.
- (33) Rochdi, N.; Tonneau, D.; Jandard, F.; Dallaporta, H.; Safarov, V.; Gautier, J. Electrical conductivity of ultra-thin silicon nanowires. *Journal of Vacuum Science & Technology B: Microelectronics and Nanometer Structures Processing, Measurement, and Phenomena* **2008**, 26 (1), 159–163.
- (34) Centrone, A. Infrared Imaging and Spectroscopy Beyond the Diffraction Limit. *Annual Review of Analytical Chemistry* **2015**, 8 (1), 101–126.
- (35) Levratovsky, Y.; Gross, E. High spatial resolution mapping of chemically-active self-assembled N-heterocyclic carbenes on Pt nanoparticles. *Faraday Discuss.* **2016**, *188* (0), 345–353.
- (36) Karst, J.; Sterl, F.; Linnenbank, H.; Weiss, T.; Hentschel, M.; Giessen, H. Watching in situ the hydrogen diffusion dynamics in magnesium on the nanoscale. *Sci. Adv.* **2020**, *6* (19), eaaz0566.
- (37) Stan, G.; King, S. W. Atomic force microscopy for nanoscale mechanical property characterization. *J. Vac. Sci. Technol. B* **2020**, 38 (6), No. 060801.
- (38) Dazzi, A.; Prazeres, R.; Glotin, F.; Ortega, J. M. Analysis of nano-chemical mapping performed by an AFM-based ("AFMIR") acousto-optic technique. *Ultramicroscopy* **2007**, *107* (12), 1194–1200
- (39) Moore, S. L.; Ciccarino, C. J.; Halbertal, D.; McGilly, L. J.; Finney, N. R.; Yao, K.; Shao, Y.; Ni, G.; Sternbach, A.; Telford, E. J.; Kim, B. S.; Rossi, S. E.; Watanabe, K.; Taniguchi, T.; Pasupathy, A. N.; Dean, C. R.; Hone, J.; Schuck, P. J.; Narang, P.; Basov, D. N. Nanoscale lattice dynamics in hexagonal boron nitride moiré superlattices. *Nat. Commun.* **2021**, *12* (1), 5741.
- (40) Jiang, J.-H.; Xu, X. G.; Gilburd, L.; Walker, G. C. Optical hotspots in boron-nitride nanotubes at mid infrared frequencies: one-dimensional localization due to random-scattering. *Opt. Express* **2017**, 25 (21), 25059–25070.
- (41) Dai, S.; Fei, Z.; Ma, Q.; Rodin, A. S.; Wagner, M.; McLeod, A. S.; Liu, M. K.; Gannett, W.; Regan, W.; Watanabe, K.; Taniguchi, T.; Thiemens, M.; Dominguez, G.; Neto, A. H. C.; Zettl, A.; Keilmann, F.; Jarillo-Herrero, P.; Fogler, M. M.; Basov, D. N. Tunable Phonon Polaritons in Atomically Thin van der Waals Crystals of Boron Nitride. *Science* **2014**, *343* (6175), 1125–1129.
- (42) Geick, R.; Perry, C. H.; Rupprecht, G. Normal Modes in Hexagonal Boron Nitride. *Phys. Rev.* **1966**, 146 (2), 543–547.
- (43) Caldwell, J. D.; Kretinin, A. V.; Chen, Y.; Giannini, V.; Fogler, M. M.; Francescato, Y.; Ellis, C. T.; Tischler, J. G.; Woods, C. R.; Giles, A. J.; Hong, M.; Watanabe, K.; Taniguchi, T.; Maier, S. A.; Novoselov, K. S. Sub-diffractional volume-confined polaritons in the natural hyperbolic material hexagonal boron nitride. *Nat. Commun.* 2014, 5, 5221.
- (44) Huang, T.-X.; Cong, X.; Wu, S.-S.; Lin, K.-Q.; Yao, X.; He, Y.-H.; Wu, J.-B.; Bao, Y.-F.; Huang, S.-C.; Wang, X.; Tan, P.-H.; Ren, B. Probing the edge-related properties of atomically thin  $MoS_2$  at nanoscale. *Nat. Commun.* **2019**, *10* (1), 5544.
- (45) Lyu, B.; Li, H.; Jiang, L.; Shan, W.; Hu, C.; Deng, A.; Ying, Z.; Wang, L.; Zhang, Y.; Bechtel, H. A.; Martin, M. C.; Taniguchi, T.; Watanabe, K.; Luo, W.; Wang, F.; Shi, Z. Phonon Polariton-assisted Infrared Nanoimaging of Local Strain in Hexagonal Boron Nitride. *Nano Lett.* **2019**, *19* (3), 1982–1989.
- (46) He, L. N.; Wang, D. M.; Hasegawa, S. A study of plasmadeposited amorphous  $SiO_x$ :H ( $0 \le x \le 2.0$ ) films using infrared spectroscopy. *J. Non-Cryst. Solids* **2000**, 261 (1), 67–71.
- (47) Socrates, G. Infrared and Raman Characteristic Group Frequencies: Tables and Charts; John Wiley & Sons: 2004.
- (48) San Andrés, E.; del Prado, A.; Martínez, F. L.; Mártil, I.; Bravo, D.; López, F. J. Rapid thermal annealing effects on the structural properties and density of defects in SiO<sub>2</sub> and SiN<sub>x</sub>:H films deposited by electron cyclotron resonance. *J. Appl. Phys.* **2000**, *87* (3), 1187–1192.

- (49) Mawhinney, D. B.; Glass, J. A.; Yates, J. T. FTIR Study of the Oxidation of Porous Silicon. *J. Phys. Chem. B* **1997**, 101 (7), 1202–1206.
- (50) Oh, T.; Choi, C. K. Comparison Between SiOC Thin Film by Plasma Enhance Chemical Vapor Deposition and  $SiO_2$  Thin Film by Fourier Transform Infrared Spectroscopy. *Journal of The Korean Physical Society* **2010**, *56* (4), 1150–1155.
- (51) Pai, P. G.; Chao, S. S.; Takagi, Y.; Lucovsky, G. Infrared spectroscopic study of SiOx films produced by plasma enhanced chemical vapor deposition. *Journal of Vacuum Science & Technology A* **1986**, 4 (3), 689–694.
- (52) Patel, N.; Mariazzi, S.; Toniutti, L.; Checchetto, R.; Miotello, A.; Dirè, S.; Brusa, R. S. Structural evolution of nanoporous silica thin films studied by positron annihilation spectroscopy and Fourier transform infrared spectroscopy. *J. Phys. D: Appl. Phys.* **2007**, 40 (17), 5266–5274.
- (53) Dorn, R. W.; Ryan, M. J.; Kim, T.-H.; Goh, T. W.; Venkatesh, A.; Heintz, P. M.; Zhou, L.; Huang, W.; Rossini, A. J. Identifying the Molecular Edge Termination of Exfoliated Hexagonal Boron Nitride Nanosheets with Solid-State NMR Spectroscopy and Plane-Wave DFT Calculations. *Chem. Mater.* **2020**, 32 (7), 3109–3121.
- (54) Ryu, G. H.; Park, H. J.; Ryou, J.; Park, J.; Lee, J.; Kim, G.; Shin, H. S.; Bielawski, C. W.; Ruoff, R. S.; Hong, S.; Lee, Z. Atomic-scale dynamics of triangular hole growth in monolayer hexagonal boron nitride under electron irradiation. *Nanoscale* **2015**, 7 (24), 10600–10605.
- (55) Mouhoub, O.; Martinez-Gordillo, R.; Nelayah, J.; Wang, G.; Park, J.-H.; Kim, K.; Kang; Lee, Y.; Hee; Bichara, C.; Loiseau, A.; Ricolleau, C.; Amara, H.; Alloyeau, D. Quantitative insights into the growth mechanisms of nanopores in hexagonal boron nitride. *Phys. Rev. Mater.* **2020**, *4* (1), No. 014005.
- (56) Liu, S.; Comer, J.; van Duin, A. C. T.; van Duin, D. M.; Liu, B.; Edgar, J. H. Predicting the preferred morphology of hexagonal boron nitride domain structure on nickel from ReaxFF-based molecular dynamics simulations. *Nanoscale* **2019**, *11* (12), 5607–5616.
- (57) Galeener, F. L.; Lucovsky, G.; Mikkelsen, J. C. Vibrational spectra and the structure of pure vitreous B2O3. *Phys. Rev. B* **1980**, 22 (8), 3983–3990.
- (58) Jun, L.; Shuping, X.; Shiyang, G. FT-IR and Raman spectroscopic study of hydrated borates. Spectrochimica Acta Part A: Molecular and Biomolecular Spectroscopy 1995, 51 (4), 519–532.
- (59) Richards, D.; Zayats, A.; Royer, P.; Barchiesi, D.; Lerondel, G.; Bachelot, R. Near-field optical patterning and structuring based on local-field enhancement at the extremity of a metal tip. *Philosophical Transactions of the Royal Society of London. Series A: Mathematical, Physical and Engineering Sciences* **2004**, 362 (1817), 821–842.
- (60) Nash, D. J.; Chagoya, K. L.; Felix, A.; Torres-Davila, F. E.; Jiang, T.; Le, D.; Tetard, L.; Rahman, T. S.; Blair, R. G. Analysis of the fluorescence of mechanically processed defect-laden hexagonal boron nitride and the role of oxygen in catalyst deactivation. *Advances in Applied Ceramics* **2019**, *118* (4), 153–158.